ELSEVIER

International Journal of Heat and Fluid Flow 21 (2000) 627–639

International Journal of
HEAT AND
FLUID FLOW

www.elsevier.com/locate/ijhff

DNS, experimental and modelling study of axially compressed in-cylinder swirling flow

S. Jakirlić [a,*], J. Volkert [b], H. Pascal [b,c], K. Hanjalić [c], C. Tropea [a]

[a] *Fachgebiet Strömungslehre und Aerodynamik, Darmstadt University of Technology, Petersenstrasse 30, 64287 Darmstadt, Germany*
[b] *Lehrstuhl für Strömungsmechanik, University of Erlangen, Cauerstrasse 4, 91058 Erlangen, Germany*
[c] *Faculty of Applied Physics, Delft University of Technology, Lorentzweg 1, 2628 CJ Delft, The Netherlands*

Abstract

The paper reports on recent progress in the investigation and modelling of joint effects of compression and swirl on turbulence in a cylinder of a single-stroke rapid compression machine (RCM). Experimental and modelling investigations cover a flat cylinder geometry and a 'squish' configuration with a bowl-in-cylinder head. In addition, the direct numerical simulations (DNS) of all three operational modes of RCM have been performed: steady rotation, transient spin-down without compression and transient spin-down with compression. The Reynolds-averaged Navier–Stokes simulation (RANS) was performed using a low-*Re*-number second-moment closure. The results obtained are compared with the experimental results and with DNS. Prior to the computation of the RCM, the applied turbulence model was validated in several generic flows relevant to the RCM: developed and developing flows in an axially rotating pipe, swirling flows in combustion chamber geometries and long straight pipes and several flows with mean compression, ranging from homogeneous compression to the compression in a closed cylinder. It is demonstrated that in all cases considered including the RCM, the applied RANS model reproduces reasonably well both the DNS and experimental results, without any model or coefficient modifications. © 2000 Begell House Inc. Published by Elsevier Science Inc. All rights reserved.

---

1. Introduction

The flows in internal combustion engines are exceedingly complex, involving strong swirls, high degrees of anisotropy, compression effects and, in the case of fired engines, interaction with the combustion process. Even restricting the attention to the isothermal case, large differences can be found between the predictions of the same flow using different codes and turbulence models – a situation which is highly unsatisfactory from the viewpoint of the engine developer (e.g., Dupeuble et al., 1994).

In this paper, we present some results of experimental and numerical investigations of the time-dependent, in-cylinder flow encountered in the rapid compression machine (RCM). The main goal of the study is to gain a better insight into the turbulence dynamics in a piston–cylinder assembly, primarily of the coupled effects of compression and swirl. The experimental and direct numerical simulations (DNS) results have also served to provide a database for validating and possibly improving the Reynolds-averaged Navier–Stokes simulation (RANS) models for such flows.

The RCM, Fig. 1, consists of a transparent rotating cylinder head and a stationary part accommodating a piston (Volkert et al., 1996; Keller et al., 1998). The rotating section, driven by an external motor, generates a flow rotation, which transforms into a swirl after the cylinder is suddenly stopped, thus providing a well-defined initial state of the flow prior to the piston movement, i.e., compression. Although there was no valve-intake nor discharge flow, the combined compression and the initial swirl generate complex secondary currents. The intention of the experiment was to reduce the engine flow to a simple generic situation in which the effects of two major strain rates, i.e., swirl and compression, can be studied free from interference by other phenomena. Such well-defined experimental results should serve as a basis for the validation of RANS models adressing these phenomena.

Parallel to the experiments, the DNS of all three operational modes of the RCM were performed, providing additional information which is not tractable with experimental techniques. A comprehensive data set was thus collected to enable further insight into the effects of a single-stroke, anisotropic compression and swirl on the evolution of turbulence and to provide a basis for assessment of RANS models.

The following sections briefly describe the experimental and solution methods used. It will be followed by the results of some test cases accounting separately for rotating swirl and mean flow compression effects. Finally a selection of results for all three RCM cases will be presented.

---

[*] Corresponding author. Tel.: +49-6151-16-3554; fax: +49-6151-16-4754.
E-mail address: jsuad@hrzpub.tu-darmstadt.de (S. Jakirlić).

PII: S0142-727X(00)00054-0

Notation

A	Lumley's (1978) two-componentality factor, $A = 1 - 9/8(A_2 - A_3)$
A_2	second invariant of a_{ij}, $A_2 = a_{ij}a_{ji}$
A_3	third invariant of a_{ij}, $A_3 = a_{ij}a_{jk}a_{ki}$
a_{ij}	Reynolds-stress anisotropy tensor, $a_{ij} = \overline{u_i u_j}/k - 2/3\delta_{ij}$
D	diameter of RCM cylinder, $D = 75$ mm
$d_{\rm p}$	diameter of seeding particles (oil droplets)
E	Lumley's (1978) two-componentality factor, $E = 1 - 9/8(E_2 - E_3)$
E_2	second invariant of e_{ij}, $E_2 = e_{ij}e_{ji}$
E_3	third invariant of e_{ij}, $E_3 = e_{ij}e_{jk}e_{ki}$
e_{ij}	dissipation anisotropy tensor, $e_{ij} = \varepsilon_{ij}/\varepsilon - 2/3\delta_{ij}$
k	turbulent kinetic energy, $k = 1/2\overline{u_i u_i}$
$L(t)$	instantaneous clearance height
L_0	clearance height at BDC, $L_{\rm BDC} = 200$ mm for flat configuration of RCM
$L_{\rm TDC}$	clearance height at TDC (denoted also as $Z_{\rm c}$), $L_{\rm TDC} = 40$ mm for flat and $L_{\rm TDC} = 75$ mm for bowl configuration of RCM
N	rotation rate, $N = W_{\rm wall}/U_{\rm b}$
$n_{\rm wall}$	rotational speed (rpm)
$P, \overline{P}, p$	momentary, mean and fluctuating pressure
R	cylinder radius ($R = D/2$)
$Re_{\rm t}$	Reynolds number of turbulence, $Re_{\rm t} = k^2/\nu\varepsilon$
$Re_{\rm w}$	Reynolds number, $Re_{\rm w} = W_{\rm wall}D/\nu$
Ri	Richardson number, $Ri = 2(W/r^2)(\partial(rW)/\partial r)/[(\partial U/\partial r)^2 + (r\partial(W/r)/\partial r)]$
r, φ, z	cylindrical coordinates
S	compression strain rate, $S = U_{\rm p}(t)/L(t) = (1/\rho)\,{\rm d}\rho/{\rm d}t$
$T(t)$	mean temperature
T_0	mean temperature at BDC
T_{ij}	stress tensor
t	time
$U_i, \overline{U}_i, u_i$	momentary, mean and fluctuating velocity fields
$U_{\rm b}$	bulk velocity
$U_{{\rm b}i}$	velocity of moving boundaries
$U_{\rm p}(t)$	instantaneous piston speed
U_0	maximum piston speed, $U_{\rm p}(t) = -\underline{U_0}\exp(-St)$ (RCM) or generally $U_{\rm p}(t) = -\underline{U_0}\sin(\omega t)$
$\overline{u_i u_j}$	kinematic Reynolds-stress tensor
$W_{\rm wall}$	circumferential velocity of rotating wall
W	($\equiv U_\varphi$) tangential velocity component
Z	distance measured from cylinder head
$Z_{\rm c}$	see $L_{\rm TDC}$

Greeks

δ_{ij}	Kronecker delta
ε	dissipation rate of k
ε_{ij}	dissipation rate tensor
$\epsilon_{\rm c}$	compression ratio, $\epsilon_{\rm c} = L_0/L_{\rm TDC}$
Φ_{ij}	redistribution term in the transport equation for $\overline{u_i u_j}$
$\nu(t)$	kinematic viscosity
ν_0	kinematic viscosity at BDC
$\rho(t)$	mean density
ρ_0	mean density at BDC

Abbreviations

BDC	bottom dead centre (begin of the compression stroke)
CA	crank angle
DNS	direct numerical simulation
RANS	Reynolds-averaged Navier–Stokes
RCM	rapid compression machine
TDC	top dead centre (end of the compression stroke)

2. Experimental method

2.1. Apparatus – rapid compression machine

The operation of the apparatus consists primarily of two phases. While the first phase is related to the generation of swirl inside the cylinder through cylinder rotation, an axial compression of the swirling flow is realized in the second phase.

As shown in Fig. 1, the rotating part (including the cylinder head) is driven by an external DC motor. This rotating part of the cylinder is separated from the non-rotating part by a small gap ($\Delta z = 1$ mm). The initial swirl intensity is controlled by the rotation rate of the cylinder. Experiments have been performed at 30, 300, 1200 and 1800 rpm. After stopping the cylinder rotation, the swirling flow in the cylinder is subjected to an axial compression by a hydraulically driven piston. The compression ratio has been fixed to a value of $\epsilon_{\rm c} = 5.0$. The compression strain rate S, defined as the ratio of the instantaneous piston speed $U_{\rm p}(t)$ and the length of the current volume to be compressed ($L(t)$),

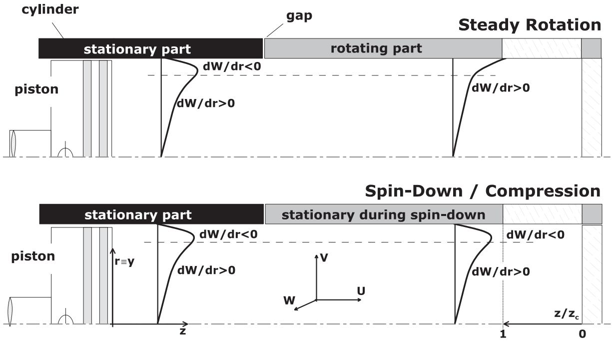

Fig. 1. Design of the RCM.

$$S = \frac{1}{L(t)}\frac{{\rm d}z_{\rm p}}{{\rm d}t} = \frac{U_{\rm p}(t)}{L(t)}, \tag{1}$$

was varied in the range of $0.0 \leqslant S \leqslant 11.5$ s^{-1}. Since the piston velocity can be controlled by the hydraulic system, an exponentially decaying velocity was imposed, corresponding to a constant strain rate during the entire compression stroke (theoretically, $U_{\rm p}(t) = U_0\exp(-St)$). The non-rotating section of the cylinder serves as an acceleration distance for the piston, to reach the desired initial compression velocity when passing the gap. For optical access, the cylinder head is made of high quality polished quartz glass.

As shown in Fig. 1 an auxiliary axial coordinate denoted by Z is used for displaying the measurements performed in the cylinder head, since the reference was the head surface, not the piston.

2.2. Laser doppler anemometer (LDA)

A four-beam, two-component backscatter LDA (5 W Ar-ion laser, $\lambda = 488/514.5$ nm) with measurement volumes of 25.8 μm and 27.2 μm was used for velocity measurements. The scattered light was directed to color separation optics, directly connected to photomultipliers. After passing the signals through a two-channel downmixer and bandpass filters, counter processors (TSI 1990/1980) were used for signal processing. Oil droplets (mixture 1:1) with diameters of $d_{\mathrm{p}} \leqslant 1$ μm were used for seeding, being injected through the gap during the spin-up phase. Since the experiment is a one-shot event, all data acquisition was synchronized to the cylinder stop signal. Cycle-resolved averaging was performed with time domain filtering (spline smoothing) of the in-cycle velocity time series. Up to 200 repetitions were performed to build statistics about the flow field. Thus, the mean velocity refers to the time mean velocity for the case of steady cylinder rotation, but to a phase mean velocity for all other measurements. Further details of the experimental facility, including also estimation of experimental uncertainties, can be found in the work of Volkert (1999).

3. Computational methods

Both computational methods applied, DNS and RANS, were used for simulation of all three operational modes of the RCM:

- steady rotation of the cylinder, i.e., generation of the initial swirl ($\partial/\partial t = 0$),
- spin-down (flow evolution after cylinder rotation is abruptly stopped),
- spin-down with compression (effects of one-dimensional (1-D) compression on the swirling flow).

The simultaneous action of a swirl about the cylinder axis and a compression along its axis impose a complex strain with two shear components, $\partial U/\partial r$ and $\partial W/\partial r$, and streamline curvature through the additional strain $-W/r$. In addition, there is an enhanced irrotational mean strain rate $\partial U/\partial z$ imposed by the piston displacement. The piston movement leads to a reduction of the fluid volume, thus suppressing the spreading of turbulent structures and diminishing the integral length scales. Other important features are a strong departure from the local equilibrium and strong anisotropies of both the Reynolds-stress and dissipation rate tensors.

The following sections briefly describe the solution methods used. First, the governing equations describing the flow encountered in the piston–cylinder configuration are presented. It is followed by a description of the numerical methods used for DNS and RANS, and the discussion of the turbulence models applied.

3.1. Governing equations

The continuity and Navier–Stokes equations governing the flow in the RCM take the following form in the coordinate frame moving with the piston:

$$\frac{\mathrm{d}}{\mathrm{d}t}\int_V \rho \, \mathrm{d}V + \int_S \rho (U_i - U_{\mathrm{b}i}) n_i \, \mathrm{d}S = 0, \tag{2}$$

$$\frac{\mathrm{d}}{\mathrm{d}t}\int_V \rho U_i \, \mathrm{d}V + \int_S \rho U_i (U_j - U_{\mathrm{b}j}) n_j \, \mathrm{d}S = \int_S T_{ji} n_j \, \mathrm{d}S, \tag{3}$$

where $U_{\mathrm{b}i}$ stands for the velocities of moving boundaries of the computational domain. In the case of 1-D compression $U_{\mathrm{b}i} = (U_{\mathrm{p}},\ 0,\ 0)$, where U_{p} represents the piston velocity. Details of the numerical methods used, accounting for the piston movement, are given in Sections 3.2 and 3.3.

The stress tensor T_{ij} in cartesian coordinates is given by

$$T_{ij} = -P\delta_{ij} + \mu\left(\frac{\partial U_i}{\partial x_j} + \frac{\partial U_j}{\partial x_i}\right) - \frac{2}{3}\mu\frac{\partial U_k}{\partial x_k}\delta_{ij}. \tag{4}$$

For the RANS computations, the Reynolds decomposition of all momentary variables was applied ($U_i = \overline{U}_i + u_i$, $P = \overline{P} + p$), yielding the ensemble averaged stress tensor

$$\overline{T}_{ij} = -\overline{P}\delta_{ij} + \mu\left(\frac{\partial \overline{U}_i}{\partial x_j} + \frac{\partial \overline{U}_j}{\partial x_i}\right) - \frac{2}{3}\mu\frac{\partial \overline{U}_k}{\partial x_k}\delta_{ij} - \rho\overline{u_i u_j}. \tag{5}$$

The Reynolds-stress tensor $-\rho\overline{u_i u_j}$ is to be approximated by an appropriate turbulence model.

By assuming that acoustic waves have an insignificant effect on the turbulence (e.g., Reynolds, 1980; Wu et al., 1985), the fluctuating field can be viewed as being incompressible ($\partial u_i/\partial x_i = 0$), interacting with a compressed mean flow. The mean gas density changes during the compression and is approximated as being only a function of time and temperature. The time variation of viscosity is accounted for by a power-law (see e.g., White, 1974). For adiabatic compression these relations are

$$\left[\frac{\rho(t)}{\rho_0}\right]^{\kappa-1} = \frac{T(t)}{T_0}, \qquad \frac{\mu(t)}{\mu_0} = \left[\frac{T(t)}{T_0}\right]^{0.75}, \tag{6}$$

where in both equations the index '0' refers to the beginning of the compression process. The homogeneous density also implies a homogeneous divergence of the mean velocity so that the terms in the momentum equations (13) representing molecular momentum transport are free of dilatational effects.

3.2. The DNS procedure

All DNS results presented were obtained by the FLOWSI code developed by Friedrich and coworkers at TU Munich (see e.g., Schmitt, 1982; Güntsch, 1996). FLOWSI is based on the finite volume numerical method for solving Navier–Stokes equations in a (r, φ, z) cylindrical coordinate system with staggered variable arrangement.

The three-dimensional (3-D) geometry, meshed by a uniform distribution of finite volumes $\mathrm{d}V = \mathrm{d}r\, r\mathrm{d}\varphi\, \mathrm{d}z$, has the shape of a straight circular cylinder which is compressed in the z-direction. Actually, during the compression stroke, the following transformation of the axial coordinate z is used in order to conserve the number of cells

$$z(t) = \zeta L(t) \quad \text{with } 0 \leqslant \zeta \leqslant 1, \tag{7}$$

where $L(t)$ is the clearance height (i.e., the instantaneous length of the cylinder). The space and time derivatives can then be written as

$$\frac{\partial}{\partial z} \to \frac{1}{L(t)}\frac{\partial}{\partial \zeta}, \quad \frac{\partial}{\partial t} \to \frac{\partial}{\partial t} \underbrace{+ \frac{\zeta}{L(t)}|U_{\mathrm{p}}(t)|}_{-U_{\mathrm{mesh}}} \frac{\partial}{\partial \zeta}, \tag{8}$$

where $U_{\mathrm{p}}(t) = \mathrm{d}L(t)/\mathrm{d}t$ is the piston velocity.

The Navier–Stokes equations are transformed according to Eq. (8) and are integrated over all finite control volumes $\mathrm{d}V$. The convection relative to the moving mesh is represented by the term $-U_{\mathrm{mesh}}\partial/\partial\zeta$. The equations also contain extra terms which account for the time-dependency of the axial coordinate z. Furthermore, an important contribution from the time-variation of the mean gas density $\rho(t)$ comes from the unsteady term in the governing equations. The space discretisation scheme is second order accurate.

In order to provide the proper coupling between the pressure and velocity fields, the resulting equations are solved using a combination of staggered grids $(\underset{\sim}{x}; \underset{\sim}{\hat{x}})$, and a non-iterative fractional time-step algorithm. First a tentative velocity field $\mathbf{u}^*$

is obtained in order to satisfy the continuity equation at each new time step (denoted by the superscript $n+1$). This velocity field is then updated only once from the following expression:

$$\mathbf{u}^{n+1} = \mathbf{u}^{*} - \frac{\Delta t}{\rho}\nabla p^{*}. \tag{9}$$

The pressure-like variable p^{*} is obtained by solving the equation

$$-\frac{1}{\rho}\nabla\cdot\nabla p^{*} = \nabla\cdot\mathbf{u}^{*} + \underbrace{\frac{1}{\rho}\frac{\partial\rho}{\partial t}}_{\text{mean compression}}. \tag{10}$$

As the φ-axis is a direction of statistical symmetry in this cylindrical computational domain, periodicity is assumed and fast Fourier transforms of the discretised equation (10) are performed in this spatial direction. The resulting set of two-dimensional (2-D) Helmholtz equations is solved by the direct inversion of the associated tri-diagonal matrix system (Schumann and Sweet, 1976), which makes this vectorised code quite efficient.

An essentially explicit time-marching process, based on a second-order accurate combination of Euler and leap-frog schemes, is used. Some computational efforts could be saved by reducing the time-step limitations which ensure the numerical stability, in particular, close to the cylinder axis. An implicit treatment of all the linearised convective terms and the diffusive terms containing derivatives in the φ-direction has been implemented (Eggels et al., 1994).

The no-slip and impermeability boundary conditions are imposed in a different but consistent way for each velocity component. The difference originates from the use of the staggered grids $(\underline{x};\underline{\hat{x}})$. Neumann boundary conditions are implemented for the pressure solver since a boundary condition is set for the normal velocity component.

3.3. RANS approach: numerical method and turbulence model

In order to conserve the number of mesh cells during the compression stroke, the so called *space conservation law* (SCL, Demirdžić and Perić, 1990) is applied. The method, incorporated into a finite volume procedure, involves the solving of an additional equation describing conservation of space simultaneously with the continuity and momentum equations. For a spatial region of volume V bounded by a closed surface S, this new equation is

$$\frac{\mathrm{d}}{\mathrm{d}t}\int_V \mathrm{d}V - \int_S U_{\mathrm{b}i} n_i \,\mathrm{d}S = 0. \tag{11}$$

In principle, all swirling flow cases considered are 3-D, involving all three velocity components and all six Reynolds-stress components. However, we applied the axisymmetric approximation $(\partial/\partial\varphi = 0)$, which simplifies to a large degree computational efforts reducing the differential Reynolds averaged continuity and momentum equations to the following form:

$$\frac{\partial\rho}{\partial t} + \frac{\rho}{r}\frac{\partial\left[r\left(\overline{U}_j - U_{\mathrm{b}j}\right)\right]}{\partial x_j} = 0, \tag{12}$$

$$\frac{\partial(\rho\overline{U}_i)}{\partial t} + \frac{\rho}{r}\frac{\partial\left[r\overline{U}_i\left(\overline{U}_j - U_{\mathrm{b}j}\right)\right]}{\partial x_j} = -\frac{\partial\overline{P}}{\partial x_i} + \frac{1}{r}\frac{\partial}{\partial x_j}\left[r\left(\mu\frac{\partial\overline{U}_i}{\partial x_j} - \rho\overline{u_i u_j}\right)\right] + \rho S_{\overline{U}_i}, \tag{13}$$

where the vector $x_i(r,z)$ denotes the coordinate directions and $U_i(U_r, U_\varphi, U_z)$ $(\equiv (V, W, U))$ stands for the mean velocity vector (Fig. 1). As seen from Eq. (13), only the convective parts are to be modified by the piston movement. The source terms $S_{\overline{U}_i}$ arising from the coordinate transformation are given in Table 1.

Table 1
Sources of momentum equations

$S_{\overline{U}_i}$	Convection	Viscous diffusion	Turbulent diffusion
$S_{\overline{U}}$	–	–	–
$S_{\overline{V}}$	$+\overline{W}^2/r$	$-\nu\overline{V}/r^2$	$+\overline{w^2}/r$
$S_{\overline{W}}$	$-\overline{V}\,\overline{W}/r$	$-\nu\overline{W}/r^2$	$-\overline{wv}/r$

All RANS computations were performed by a computer code based on a finite volume numerical method for solving 2-D, RANS equations in orthogonal coordinate systems using a cell centered (collocated) variable arrangement. The primary variables are the cartesian velocity and Reynolds-stress tensor components and pressure. The velocity–pressure coupling is ensured by the pressure-correction method based on the SIMPLE algorithm (Patankar and Spalding, 1972; Rhie and Chow, 1983). Diffusion fluxes are approximated by central differences (CD). A blended upwind-central differencing scheme in the so-called differred-correction manner (Khosla and Rubin, 1974), was used for the discretisation of convective terms in all transport equations. The contribution of the CD scheme was kept as high as possible, typically 70–100% for all variables in most of the flow cases considered. The first-order, fully implicit Euler scheme was used for time stepping. For some compressed flow cases, a second-order, three time-levels time-stepping scheme was also used, but results show no noticeable difference. The equations are linearised and solved sequentially using the strongly implicit method of Stone (1968). The works of Demirdžić and Perić (1990) and Obi et al. (1991) should be consulted for further details about the numerical scheme used.

The computational domain had the shape of a straight cylinder enabling 2-D computations in a cylindrical coordinate frame. The solutions were obtained by using a non-uniform mesh, clustered near the walls, so that the values of y^+ for the point closest to the wall was about $\leqslant 0.5$.

The unknown Reynolds-stress tensor $(-\rho\overline{u_i u_j})$ in the equations of motion (13) is provided from a statistical turbulence model. Several different turbulence models have been explored in the framework of this project, ranging from the standard high-*Re*-number k–ε model (see e.g., Launder and Spalding, 1974) and its low-*Re*-number versions (Launder and Sharma, 1974; Chien, 1982), to several differential second-moment (Reynolds-stress) closures. The standard k–ε model was initially tested because it is the most widely used model in industrial computations of IC engines. However, without further elaboration, it can be stated that such simple eddy-viscosity model cannot capture essential features of this flow, in which swirl and compression effects lead to strong anisotropy of both the stress and dissipation tensors. This is also true of wall functions, as illustrated in Fig. 2, which presents measured and computed near-wall profiles of the tangential and axial velocity for the spin-down cases without and with compression.

Fig. 2 demonstrates that there is a dramatic departure from the equilibrium linear and logarithmic mean velocity distributions, illustrating the necessity to integrate the governing equations to the wall. For these reasons, we have adopted a low-*Re*-number Reynolds-stress model (denoted as Hanjalić, Jakirlić (HJ) low-*Re* RSM), based on the standard $\overline{u_i u_j} - \varepsilon$ closure (Gibson and Launder, 1978), which serves as

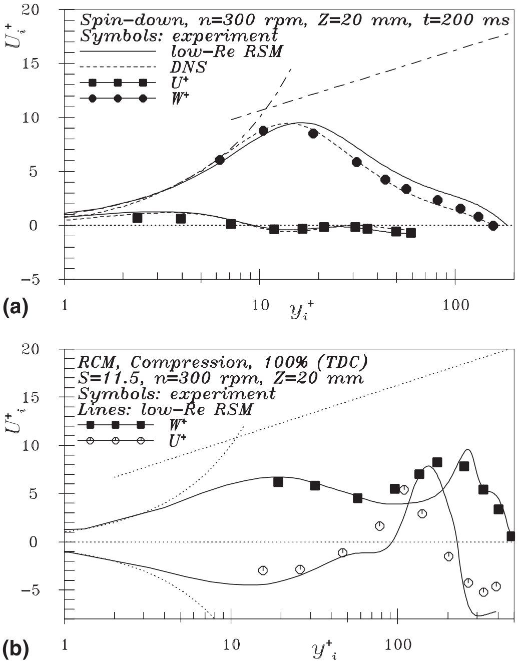

Fig. 2. Departure of the mean axial and the mean tangential velocities from the logarithmic law: spin down (a) without and (b) with compression.

the high-*Re*-number asymptote (Hanjalić et al., 1997a, 1998, 1999). The effect of viscosity, only indirectly related to the wall presence via no-slip boundary conditions (and hence, independent of the wall distance and its topology), is accounted for by introducing the viscous terms in all equations and defining the coefficients in the pressure–strain term Φ_{ij} as functions of the turbulent Reynolds number, $Re_t = k^2/(\nu\varepsilon)$. These viscous modifications are in a general form and are expected to apply both close to a wall and away from it. Wall impermeability imposes a non-viscous blockage to the fluid velocity and its fluctuations in the normal direction, causing a strong anisotropy of turbulence. This fact was exploited by introducing, in addition to Re_t, both turbulent-stress and dissipation-rate anisotropy invariants A_2, A and E as parameters in the coefficients. The use of anisotropy invariants of both tensors allows the non-viscous wall effects to be accounted for separately on the stress bearing and dissipative scales. In addition to satisfying most of the basic physical constraints, such as the asymptotic and limiting states of turbulence at vanishing and very high turbulent Reynolds numbers and the two-component limit, the model was shown to reproduce very well the mean flow and turbulence properties – particularly in the vicinity of a solid wall – in a broad variety of attached and separating non-equilibrium flows, featuring different phenomena (see e.g., (Hanjalić et al., 1997a, 1998, 1999). It should be emphasized that no additional term is introduced in the dissipation equation to account specifically for the dilatational effects, as advocated by Gosman and Watkins (1977), Reynolds (1980), Morel and Mansour (1982), nor for time changes in viscosity as proposed by El Tahry (1983). The necessity and physical arguments for including such extra terms remain still to be clarified as does the appropriate value and even the sign of the coefficients associated with them. However, based on the DNS and experimental data for the moderate compression considered here, we see no advantage in introducing such a term. The low-*Re*-number, second-moment closure model used in the present work, is summarized in Appendix A.

4. Results of flow simulations

Before presenting results for the major test case (simultaneous swirl and compression), we consider first several examples in which only one of the effects was present.

4.1. Rotating and swirling flows

Prior to the consideration of the cylinder–piston assembly, several generic types of rotating and swirling flows have been studied and computed with various RANS models. These studies were aimed at analysing the vortex dynamics and identifying some features which pose a special challenge to the turbulence modelling. The flows considered cover a range of situations which may not be directly relevant to engine flows, but enable an in-depth analysis of the flow phenomena associated with rotation and swirl: the developing and fully developed flows in an axially rotating pipe (related to the steady rotation mode), swirling flows in combustor geometries (short cylinders) and in long pipes (related to the spin-down mode, i.e., to the decay of the swirling motion), as well as several homogeneous flows subjected to rotation, but with some additional straining. For brevity, only some conclusions will be mentioned here. Generally, all computational results obtained using the present low-*Re*-number Reynolds-stress model for swirling flows entering pipe/cylinder geometries are in reasonable agreement with available experimental data. However, some shortcomings have been noted in achieving agreement with the DNS or experimental results for the $\overline{uw}$-stress component and for capturing the transition from a concentrated vortex type of the mean swirl velocity profile to the solid body rotation profile in a long straight pipe with a weak swirl. Also, the normal stress components in the core region are somewhat underpredicted and the model yields a premature flow laminarization in rotating pipes/cylinders at high rotation speeds. However, none of these discrepancies seems to affect significantly the satisfactory reproduction of the major mean flow and turbulence parameters. More details about the model performance in these flows can be found in the work of Jakirlić et al. (1998).

4.2. Compressed flows

Several cases of homogeneous compression for which the DNS results are available in the literature (Wu et al., 1985; Le Penven and Serre, 1993) were investigated before considering the compression in closed piston/cylinder assemblies. The computations with the present models and with several other models, with both the linear (Launder et al., 1975; Speziale et al., 1991 (SSG)), and non-linear pressure–strain terms, reproduced the time evolution of the turbulence kinetic energy subjected to mean compression in reasonable agreement with the DNS data (Schmid, 1996; Hanjalić et al., 1999a).

A single-stroke compression in a closed cylinder with a sinusoidal variation of the piston velocity ($U_p(t) = U_0 \sin(\omega t)$) was then investigated in parallel by both the RANS approach and DNS. Fig. 3(a) shows the phase averaged axial velocity at four selected times during a compression stroke. The compression ratio ($\epsilon_c = 4.2$) is almost identical to that investigated experimentally and with DNS in the RCM ($\epsilon_c = 5.0$). The value of rapidity Sk/ε – the ratio of the turbulent time scale to the time scale of mean motion (see e.g., Wu et al., 1985), which can serve as a measure of the ability of compression to generate turbulence, is very close to that found in real IC engines

(≈1). On the other hand this is far from the conditions under which rapid distortion theory (RDT) is valid: $Sk/\varepsilon \gg 1$ (see e.g., Hunt, 1978). The mean velocities obtained by the present low-*Re* second moment closure are compared with the results of DNS performed by Pascal (1998). It is recalled that this flow was also simulated by DNS earlier by Güntsch and Friedrich (1995). Both simulations started with homogeneous isotropic turbulence. In the first half of the compression stroke, where the fluid accelerates (approximately up to the crank angle (CA), of 90°), the velocity profiles are almost uniform except close to the wall. The generation of the turbulent shear stress and the evolution of the stress anisotropy is very slow in this phase. In the second half of the compression stroke, where the fluid decelerates, the effects of compression cause an increase in the normal-to-the-wall stress component, approaching the two other normal stress components. The anisotropy level is approximately constant in this phase. This evolution is reasonably well-captured by the model, Fig. 3(b). Separation of the flow on the cylinder wall is observed at a crank angle of about 138°. The low-*Re*-number model applied here reproduces well the onset of separation at the appropriate CA (Fig. 3(a)) and the near-wall velocity field, though it fails to capture the peak in the velocity profile predicted by DNS. It is noted that the application of a high-*Re*-number model with wall functions fails to capture the near-wall behaviour and consequently, cannot reproduce the separation in accordance with DNS findings (not shown here). Fig. 3(c) shows the streamwise and wall normal stress components at CA = 80°. The intensity of both stress components as well as their near wall behaviour are in good agreement with the DNS data.

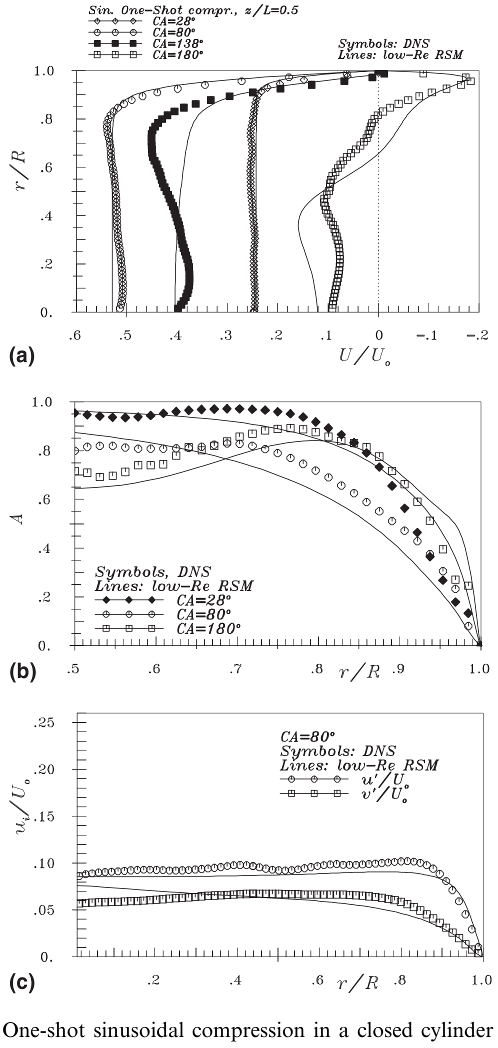

Fig. 3. One-shot sinusoidal compression in a closed cylinder – mean velocities, two componentality factors and turbulence intensities.

4.3. Flow cases in the RCM

We consider now a selection of experimental and numerical results for steady rotation, as well as spin-down flow cases without and with compression.

4.3.1. Steady rotation

The steady rotation operational mode generates swirl motion (initial flow state), which is later compressed by the piston movement. In this phase the flow is driven by the rotation of the cylinder walls, causing a strong tangential fluid motion, corresponding to the desired initial swirl intensity, and a weak axial circulation of the flow in the *r–z* plane from the piston to the cylinder head along the centerline and returning along the cylinder wall. This secondary current is induced by the non-rotating cylinder section accommodating a piston and the piston surface. Fig. 4 shows computed streamline patterns as well as measured and predicted axial and tangential velocity profiles for the steady rotation mode for both flat and bowl configurations of the RCM. The bowl configuration is a bowl-in-head and not a bowl-in-piston geometry.

The basic shapes of the profiles for both geometries are similar. However, close to the cylinder axis, a second change in the sign of the axial velocity at $Z/Z_c = 0.75$ in the bowl geometry obtained experimentally, Fig. 4(b) right, indicates the existence of a free stagnation point. The appearance of 'floating' vortices in fast rotating flows has been reported by a number of authors (e.g., Escudier, 1988) and with these investigations we hope to contribute to further enlightenment on this phenomenon. The streamline plot obtained by the model computations confirms clearly the existence of such a free swimming vortex in the core region (centerline), Fig. 4(a) right. Compared to the available experimental results, this computationally obtained bubble is obviously shifted towards the interior of the RCM. Whereas only a very weak dependency of the velocity profiles on the axial direction was documented for the flat geometry, Fig. 4(b) left, a substantial streamwise velocity gradient is observed in the bowl configuration, Fig. 4(b) right, indicating an enhancement of the axial motion in the *r–z* plane. The radial profiles of the axial velocity quantify the weak axial circulation which amounts to about 1–2% of the rotational speed for 1200 rpm.

Fig. 4(c) shows a dependency of both axial and tangential velocity profiles on rotation rates. Three rotation rates were investigated: 30, 300 and 1200 rpm. It is recalled here that for rotating pipe flows, the rotation intensity is characterized by the so called rotation rate, defined as the ratio of the tangential wall velocity to the bulk axial velocity ($N = W_{\mathrm{wall}}/U_{\mathrm{b}}$). Most experimental investigations (Murakami and Kikuyama, 1980; Hirai et al., 1988; Reich and Beer, 1989) and DNS (Eggels et al., 1994; Orlandi and Fatica, 1997) cover the range of N up to 3.5 which, according to Nishibori et al. (1987), corresponds to conditions for the flow laminarization. In the cylinder–piston configuration considered here, the rotation rate N is much higher, by more than an order-of-magnitude. Nevertheless, both the experiments and DNS show that the strong mean shear on the cylinder walls and endplate, together with a complex vortical structure, still maintains the turbulence in the cylinder, at least at the lower rotation speeds considered. The model computations reproduced the experimental flow pattern for rotational speeds up to $n_{\mathrm{wall}} = 300$ rpm ($Re_{\mathrm{w}} = 5890$, based on cylinder diameter and circumferential

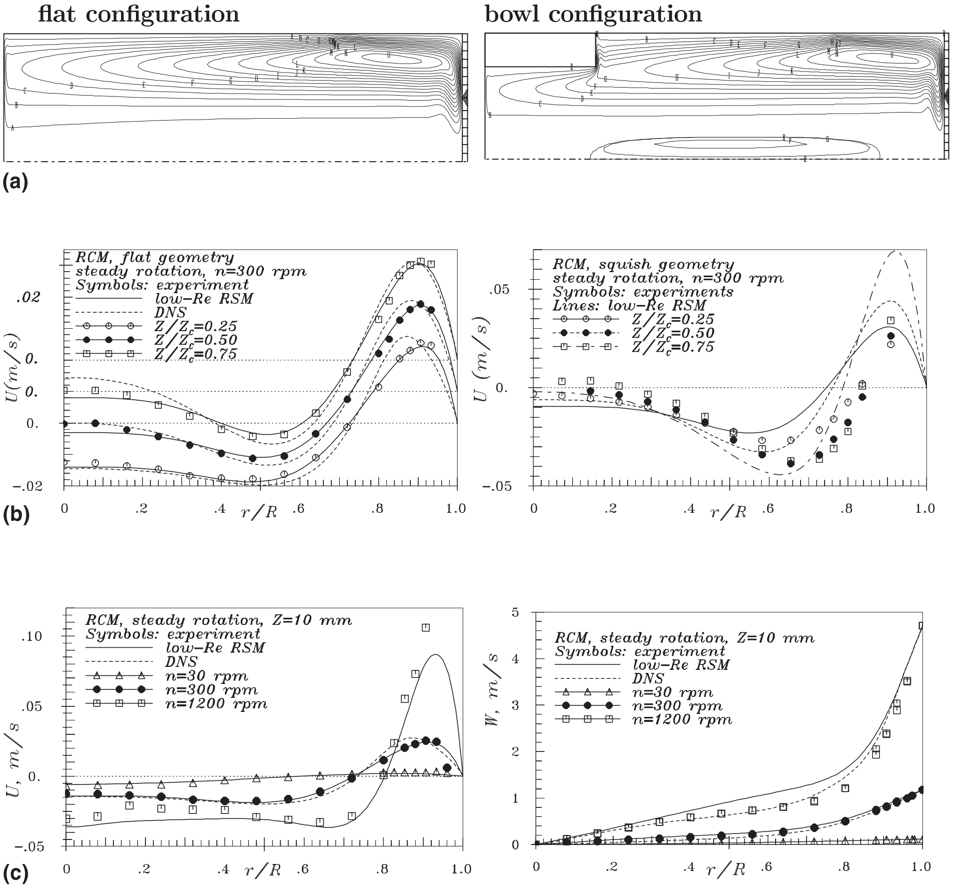

Fig. 4. Steady rotation: (a) streamline patterns for flat and bowl configurations; (b) streamwise evolution of axial velocity profiles for flat and bowl configurations; (c) dependency of axial and tangential velocity components on rotation rate for flat configuration.

velocity), as illustrated by the plot of the tangential velocity profiles. However, at higher rotation rates, the RANS computations show a complete laminarization, which leads to a weaker influence of the friction effects of the stationary part of the cylinder, and, thus, to higher swirl velocities, Fig. 4(c) right. However the difference between the computed, DNS and experimental results is not that large, implying that the real flow is also not far from laminar.

4.3.2. Spin-down flow cases

The dynamics of the decay of the swirl motion has been studied in the so called spin-down phase, which begins after the rotation of the cylinder was abruptly stopped. Two cases were considered, spin-down without compression, when the swirl decays due to the friction only, and spin-down with an anisotropic, 1-D compression. The initial turbulence field, needed for RANS computations, was taken from the experiment and was superimposed on the mean flow field corresponding to the steady rotation mode obtained computationally. This intervention was necessary in order to produce a sensible starting turbulence level, because the computations of the flow under a steady rotation produce too weak turbulence due to the afore mentioned model tendency to yield early laminarization at high rotation speeds.

Fig. 5 shows the RANS and DNS streamline patterns (computed from mean axial and radial velocity components) for three time instants during the spin-down without compression: at the very beginning of the spin-down (corresponding to the steady rotation mode) and at two later stages.

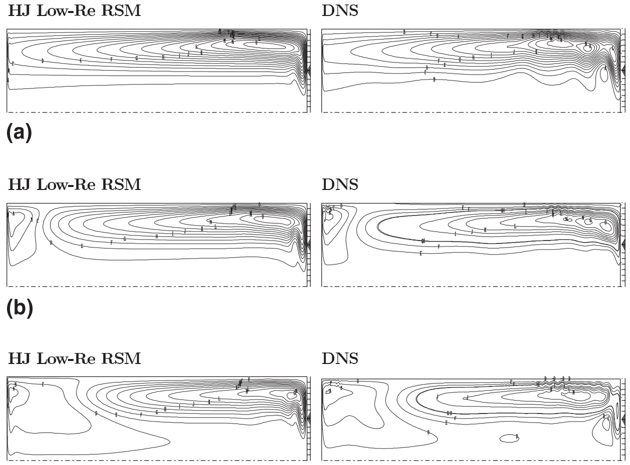

Fig. 5. Streamlines computed by HJ low-Re RSM and DNS for three selected times during the spin-down operational mode of RCM: (a) $t = 0$ ms; (b) $t = 200$ ms; (c) $t = 400$ ms.

Both the DNS and model computations predict the existence of a large vortex in the r–z plane. The vortex breaks up after the cylinder rotation is stopped, approximately at $t = 200$ ms, generating two counter-rotating vortices. After stopping of the endplate rotation, the driving force of the secondary motion, imposed by the centrifugal acceleration of fluid due to tangential motion close to the rotating endplate, disappears. A boundary layer develops at the static endplate, propagating axially into the cylinder. Therefore, the region of maximum outward radial momentum moves away from the cylinder endplate, creating an interface between the two vortex structures.

Such behaviour is in accordance with the change of the sign of the tangential velocity gradient, i.e., the Richardson number (*Ri*), from positive (steady rotation mode) to negative (spin-down mode). This vortex splitting, as well as the consequent change of the sign of the axial velocity component, is also detected in the experiment, Fig. 6.

Fig. 7 shows both the experimental and numerical (DNS and RANS) results of the phase averaged tangential velocity profiles as well as computationally obtained (RANS) velocity vectors in the *r*–*z* plane at four selected times during the compression stroke. The boundary layer on the cylinder wall separates due to the piston movement, creating ring shaped vortices. The increasing compression causes a motion of these vortices towards the core region, creating smaller eddies, which leads eventually to a more complex, dual eddy structure.

In contrast to the tangential velocities, the computed axial velocities (lines) deviate substantially from the experimental profiles (filled symbols), as shown in Fig. 8. The most likely reason is that both the RANS and DNS did not account for the outlet flow through the gap ($\Delta z = 1$ mm) between the rotating and non-rotating cylinder parts: computing the leakage through such a small gap poses a serious numerical difficulty. In the experiment, this gap, which allows a frictionless cylinder rotation, is also used for the particle seeding, Fig. 1. A comparison with the experimental data at a slightly different time (empty symbols) gives much better agreement. Although this comparison is not fully appropriate because computational and experimental results are not taken at the same time, it shows that the predicted flow fields develop in the same manner, but do so at later times relative to the piston motion. It is interesting to note that despite the deviation mentioned, the agreement between the RANS model computations and experimental tangential velocities, right-hand side of Fig. 7, is very good at all times examined. The tangential velocities show that the initial velocity profile (which appears like a wall jet), becomes strongly deformed by compression. This process starts at about 30% of the compression stroke.

This modification of the velocity field is further illustrated in Fig. 9, where the time evolution of the tangential velocity is shown for three radial positions. The characteristic modifications of the tangential velocities, observed by experiment, are captured by the model computations. The effect of compression on the mean velocity field and the ability of the model to reproduce this effect in accord with DNS results up to

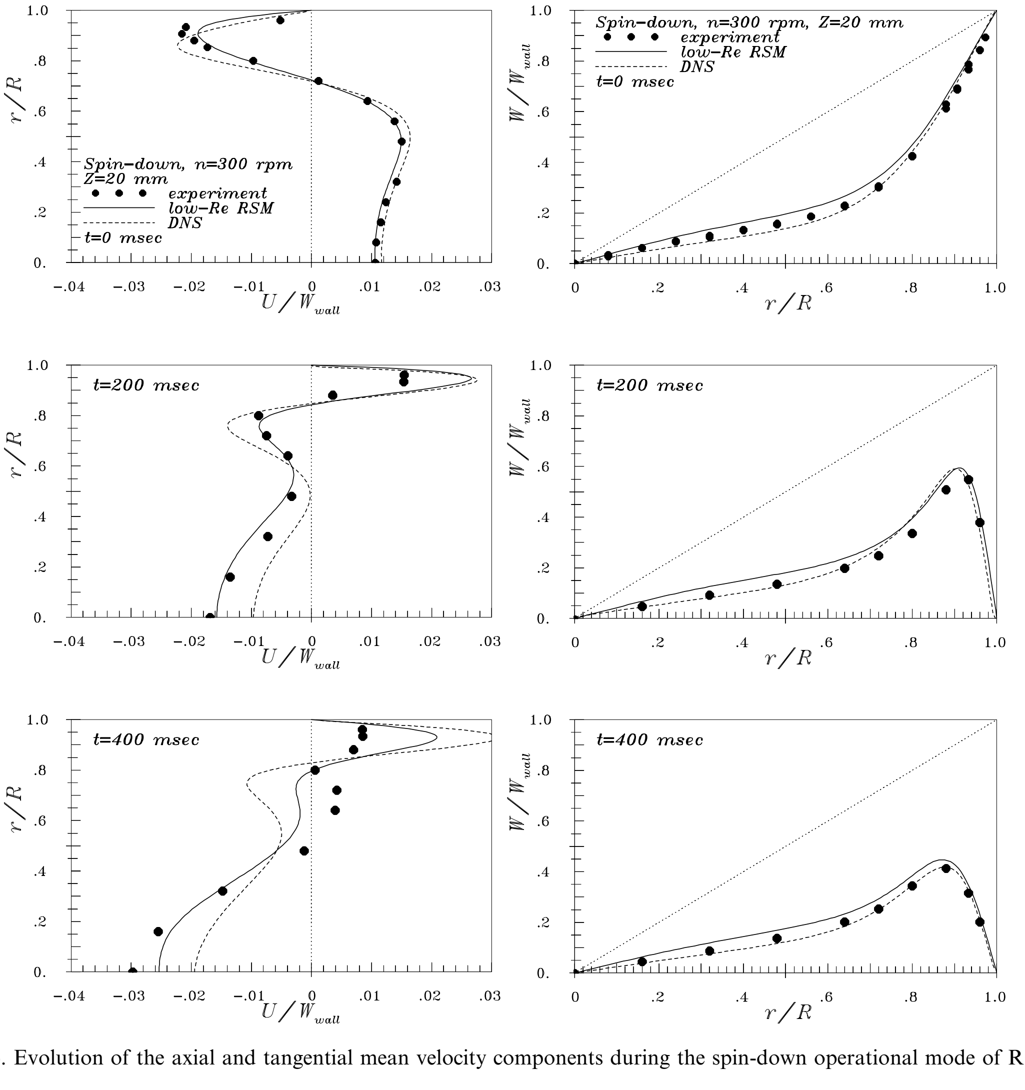

Fig. 6. Evolution of the axial and tangential mean velocity components during the spin-down operational mode of RCM.

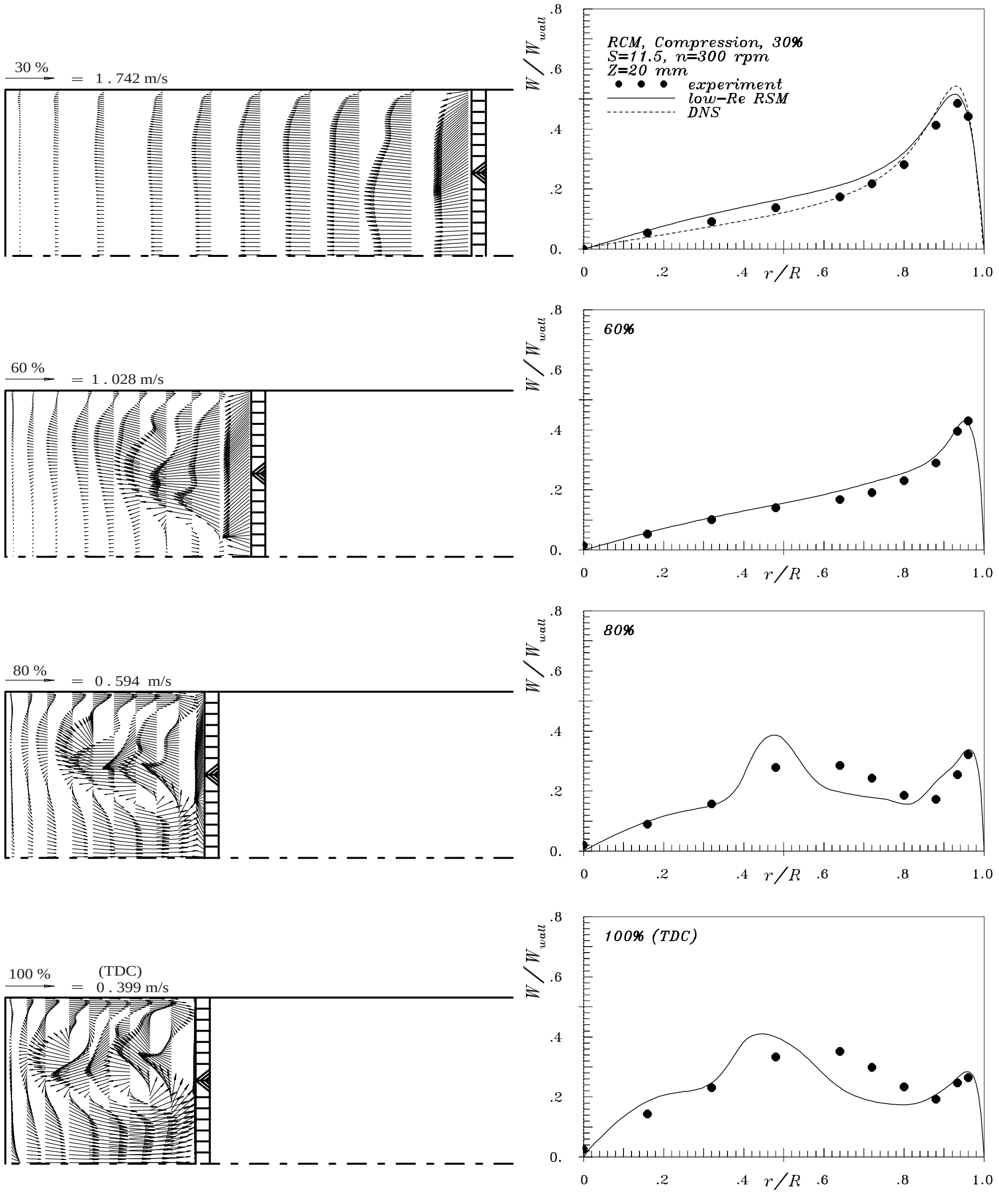

Fig. 7. Computationally (RANS) obtained velocity vector plots and tangential mean velocity profiles at selected time locations during a compression stroke of the RCM.

the wall has already been well illustrated in Fig. 2, showing very different shapes of both the axial and tangential velocity profiles in the spin-down mode without (Fig. 2(a)) and with compression (Fig. 2(b)).

5. Conclusions

The effects of swirl and compression on flow and turbulence in a piston–cylinder assembly pertinent to IC engines have been studied experimentally and numerically, the latter using the DNS and RANS approaches in parallel. The configuration considered was a single-stroke RCM in which an initially homogeneous turbulence was subjected separately and simultaneously to swirl and compression. In addition to gaining a better insight into the flow and turbulence dynamics, these investigations were also aimed at analysing the potential and prerequisites of the single-point turbulence closure for prediction of flow aerodynamics in cylinders of IC engines. The basis for the analysis is the experiments and DNS, which were performed in parallel for the same configuration. They showed that the simultaneous action of swirl and compression produces a complex flow pattern with a dual eddy structure as a consequence of vortex break-up. The flow separates at the wall at a certain crank angle and the turbulent stress field becomes highly anisotropic. Application of some popular eddy-viscosity and Reynolds-stress models showed that only the latter models have a potential for capturing the complex flow features, but require integration up to the wall. It is further shown that a low-*Re*-number second-moment closure, developed earlier and validated in a range of non-equilibrium flows (Hanjalić et al., 1997a, 1998, 1999), reproduces reasonably well the mean flow and turbulence features in all cases considered. Some interesting details

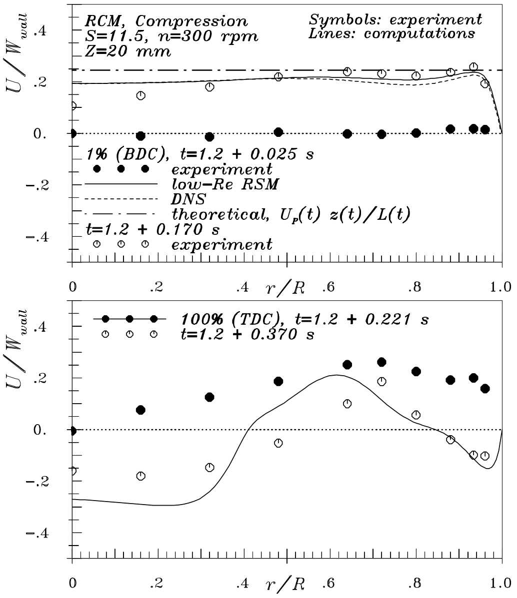

Fig. 8. Axial mean velocity profiles at the very beginning (BDC – bottom dead center) and the end (TDC – top dead center) of a compression stroke – comparison with experiment.

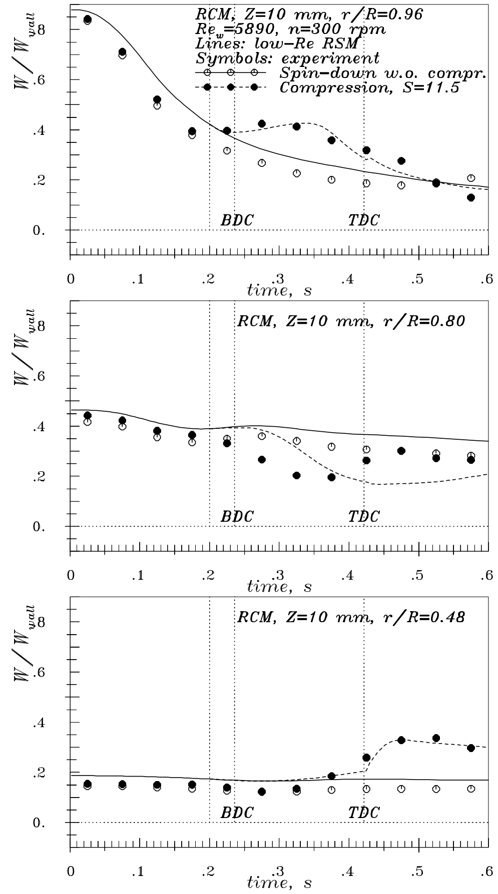

Fig. 9. Time evolution of the decaying swirl velocity during the spin-down with and without compression – comparison with experiment.

are discussed in light of the DNS evidence on the effects of flow rotation and compression.

Acknowledgements

This work was sponsored by the EC JOULE III Programme, Contract JOF3-CT95-0017 and by the DFG, Contract Tr 194/7. Dr. Pascal was supported by a TMR Marie Curie research training grant during his stay in Erlangen. A special thanks go to Prof. Friedrich, TU Munich, who generously provided his DNS code FLOWSI as a basis for these computations, as well as investing considerable time in discussing its implementation.

Appendix A. Low-Re-number second-moment closure in cylindrical coordinates

$$\frac{\partial \overline{u_iu_j}}{\partial t} + \frac{1}{r}\frac{\partial}{\partial x_k}(rU_k\overline{u_iu_j}) = D_{ij} + P_{ij} + \Phi_{ij} - \varepsilon_{ij} + S_{\overline{u_iu_j}},$$

$$\frac{\partial \varepsilon}{\partial t} + \frac{1}{r}\frac{\partial}{\partial x_k}(rU_k\varepsilon) = D_\varepsilon + C_{\varepsilon1}P_k\frac{\varepsilon}{k} - C_{\varepsilon2}f_\varepsilon\frac{\varepsilon\tilde{\varepsilon}}{k} + S_{\varepsilon_v} + S_{\varepsilon_l},$$

where

$$D_\phi = \frac{1}{r}\frac{\partial}{\partial x_k}\left[r\left(\nu\delta_{kl} + C_\phi\frac{k}{\varepsilon}\overline{u_ku_l}\right)\frac{\partial\phi}{\partial x_l}\right],$$

$$P_{ij} = -\left(\overline{u_iu_k}\frac{\partial U_j}{\partial x_k} + \overline{u_ju_k}\frac{\partial U_i}{\partial x_k}\right), \quad P_k = -\frac{1}{2}P_{ii},$$

where ϕ stands for $\overline{u_iu_j}$ and ε in corresponding equations, and the additional source terms in the stress equation $S_{\overline{u_iu_j}}$ are given for each component in Table 2.

The pressure–strain model:

$$\Phi_{ij,1} = -C_1\varepsilon a_{ij}, \quad \Phi_{ij,2} = -C_2\left(P_{ij} - \frac{2}{3}P_k\delta_{ij}\right),$$

$$\Phi^w_{ij,1} = C^w_1 f_w\frac{\varepsilon}{k}\left(\overline{u_ku_m}n_kn_m\delta_{ij} - \frac{3}{2}\overline{u_iu_k}n_kn_j - \frac{3}{2}\overline{u_ku_j}n_kn_i\right),$$

$$\Phi^w_{ij,2} = C^w_2 f_w\left(\Phi_{km,2}n_kn_m\delta_{ij} - \frac{3}{2}\Phi_{ik,2}n_kn_j - \frac{3}{2}\Phi_{kj,2}n_kn_i\right),$$

where

$$C_1 = C + \sqrt{A}E^2, \quad C = 2.5AF^{1/4}f, \quad F = \min\{0.6; A_2\},$$

$$f = \min\left\{\left(\frac{Re_t}{150}\right)^{3/2}; 1\right\}, \quad f_w = \min\left[\frac{k^{3/2}}{C_l\varepsilon x_n}; 1.4\right],$$

$$C_2 = 0.8A^{1/2}, \quad C^w_1 = \max(1 - 0.7C; 0.3), \quad C^w_2 = \min(A; 0.3),$$

$$A = 1 - \frac{9}{8}(A_2 - A_3), \quad A_2 = a_{ij}a_{ji}, \quad A_3 = a_{ij}a_{jk}a_{ki},$$

$$E = 1 - \frac{9}{8}(E_2 - E_3), \quad E_2 = e_{ij}e_{ji}, \quad E_3 = e_{ij}e_{jk}e_{ki},$$

$$a_{ij} = \frac{\overline{u_iu_j}}{k} - \frac{2}{3}\delta_{ij}, \quad e_{ij} = \frac{\varepsilon_{ij}}{\varepsilon} - \frac{2}{3}\delta_{ij}.$$

Table 2
Additional terms in the stress equation

$S_{\overline{u_i u_j}}$	Convection	Production	Viscous diffusion	Turbulent diffusion
$S_{\overline{u^2}}$	–	–	–	–
$S_{\overline{v^2}}$	$+2\overline{vw}\frac{W}{r}$	$+2\overline{vw}\frac{W}{r}$	$-2\nu\frac{\overline{v^2}-\overline{w^2}}{r^2}$	$-2C_s\frac{k}{\varepsilon}\overline{w^2}\frac{\overline{v^2}-\overline{w^2}}{r^2}-2\frac{1}{r}\frac{\partial}{\partial x}\left(C_s\frac{k}{\varepsilon}\overline{uw}\cdot\overline{vw}\right)-2\frac{1}{r}\frac{\partial}{\partial r}\left(C_s\frac{k}{\varepsilon}\overline{vw}\cdot\overline{vw}\right)$ $-2C_s\frac{1}{r}\frac{k}{\varepsilon}\left(\overline{uw}\frac{\partial\overline{vw}}{\partial x}+\overline{vw}\frac{\partial\overline{vw}}{\partial r}\right)$
$S_{\overline{w^2}}$	$-2\overline{vw}\frac{W}{r}$	$-2\overline{w^2}\frac{V}{r}$	$+2\nu\frac{\overline{v^2}-\overline{w^2}}{r^2}$	$+2C_s\frac{k}{\varepsilon}\overline{w^2}\frac{\overline{v^2}-\overline{w^2}}{r^2}+2\frac{1}{r}\frac{\partial}{\partial x}\left(C_s\frac{k}{\varepsilon}\overline{uw}\cdot\overline{vw}\right)+2\frac{1}{r}\frac{\partial}{\partial r}\left(C_s\frac{k}{\varepsilon}\overline{vw}\cdot\overline{vw}\right)$ $+2C_s\frac{1}{r}\frac{k}{\varepsilon}\left(\overline{uw}\frac{\partial\overline{vw}}{\partial x}+\overline{vw}\frac{\partial\overline{vw}}{\partial r}\right)$
$S_{\overline{uv}}$	$+\overline{uw}\frac{W}{r}$	$+\overline{uw}\frac{W}{r}-\overline{uv}\frac{V}{r}$	$-\nu\frac{\overline{uv}}{r^2}$	$-C_s\frac{k}{\varepsilon}\overline{w^2}\frac{\overline{uv}}{r^2}-\frac{1}{r}\frac{\partial}{\partial x}\left(C_s\frac{k}{\varepsilon}\overline{uw}\cdot\overline{uw}\right)-\frac{1}{r}\frac{\partial}{\partial r}\left(C_s\frac{k}{\varepsilon}\overline{vw}\cdot\overline{uw}\right)$ $-C_s\frac{1}{r}\frac{k}{\varepsilon}\left(\overline{uw}\frac{\partial\overline{uw}}{\partial x}+\overline{vw}\frac{\partial\overline{uw}}{\partial r}\right)$
$S_{\overline{uw}}$	$-\overline{uv}\frac{W}{r}$	$-\overline{uw}\frac{V}{r}$	$-\nu\frac{\overline{uw}}{r^2}$	$-C_s\frac{k}{\varepsilon}\overline{w^2}\frac{\overline{uw}}{r^2}+\frac{1}{r}\frac{\partial}{\partial x}\left(C_s\frac{k}{\varepsilon}\overline{uw}\cdot\overline{uv}\right)+\frac{1}{r}\frac{\partial}{\partial r}\left(C_s\frac{k}{\varepsilon}\overline{vw}\cdot\overline{uv}\right)$ $+C_s\frac{1}{r}\frac{k}{\varepsilon}\left(\overline{uw}\frac{\partial\overline{uv}}{\partial x}+\overline{vw}\frac{\partial\overline{uv}}{\partial r}\right)$
$S_{\overline{vw}}$	$-\left(\overline{v^2}-\overline{w^2}\right)\frac{W}{r}$	$-\overline{vw}\frac{V}{r}+\overline{w^2}\frac{W}{r}$	$-4\nu\frac{\overline{vw}}{r^2}$	$-4C_s\frac{k}{\varepsilon}\overline{w^2}\frac{\overline{vw}}{r^2}+\frac{1}{r}\frac{\partial}{\partial x}\left[C_s\frac{k}{\varepsilon}\overline{uw}(\overline{v^2}-\overline{w^2})\right]+\frac{1}{r}\frac{\partial}{\partial r}\left[C_s\frac{k}{\varepsilon}\overline{vw}(\overline{v^2}-\overline{w^2})\right]$ $+C_s\frac{1}{r}\frac{k}{\varepsilon}\left[\overline{uw}\frac{\partial}{\partial x}(\overline{v^2}-\overline{w^2})+\overline{vw}\frac{\partial}{\partial r}(\overline{v^2}-\overline{w^2})\right]$

Stress dissipation rate model:

$$\varepsilon_{ij} = f_s \varepsilon_{ij}^* + (1 - f_s)\frac{2}{3}\delta_{ij}\varepsilon,$$

$$\varepsilon_{ij}^* = \frac{\varepsilon}{k}\,\frac{\left[\overline{u_i u_j} + (\overline{u_i u_k} n_j n_k + \overline{u_j u_k} n_i n_k + \overline{u_k u_l} n_k n_l n_i n_j) f_d\right]}{1 + \frac{3}{2}\frac{\overline{u_p u_q}}{k} n_p n_q f_d},$$

$$f_s = 1 - \sqrt{A}E^2, \quad f_d = (1 + 0.1Re_{\mathrm{t}})^{-1},$$

$$f_\varepsilon = 1 - \frac{C_{\varepsilon_2} - 1.4}{C_{\varepsilon_2}}\exp\left[-\left(\frac{Re_{\mathrm{t}}}{6}\right)^2\right],$$

$$S_{\varepsilon_v} = C_{\varepsilon_3} \nu \frac{k}{\varepsilon}\overline{u_j u_k}\frac{\partial^2 U_i}{\partial x_j \partial x_l}\cdot\frac{\partial^2 U_i}{\partial x_k \partial x_l},$$

$$S_{\varepsilon_l} = \max\left\{\left[\left(\frac{1}{C_l}\frac{\partial l}{\partial x_n}\right)^2 - 1\right]\left(\frac{1}{C_l}\frac{\partial l}{\partial x_n}\right)^2; 0\right\}\frac{\varepsilon\tilde{\varepsilon}}{k}A, \quad l = \frac{k^{3/2}}{\varepsilon}.$$

Summary of the remaining coefficients

C_s	C_ε	$C_{\varepsilon 1}$	$C_{\varepsilon 2}$	$C_{\varepsilon 3}$	C_l
0.22	0.18	1.44	1.92	0.25	2.5

References

Chien, K.Y., 1982. Prediction of channel and boundary-layer flows with a low-Reynolds-number turbulence model. AIAA J. 10, 33–38.

Demirdžić, I., Perić, M., 1990. Finite volume method for prediction of fluid flow in arbitrarily shaped domains with moving boundaries. Int. J. Numer. Meth. Fluids 10, 771–790.

Dupeuble, A., Argueyrolles, B., Bailly, O., 1994. Computer simulation and comparisons of aerodynamics, mixture preparation and combustion with real engine geometries. Second periodic report, Contract JOU2-CT92-0612, Renault D.R., Rueil-Malmaison, France.

Eggels, J.G.M., Boersma, B.J., Nieuwstadt, F.T.M., 1994. Direct and large-eddy simulations of turbulent flow in an axially rotating pipe. Lab. for Aero- and Hydrodynamics, Delft University of Technology, Delft, The Netherlands, October.

El Tahry, S.H., 1983. k–ε equation for compressible reciprocating engine flows. J. Energy 7 (4), 345–353.

Escudier, M.P., 1988. Vortex breakdown: observation and explanations. Prog. Aerospace Sci. 25, 189–229.

Gibson, M.M., Launder, B.E., 1978. Ground effects on pressure fluctuations in the atmospheric boundary layer. J. Fluid Mech. 86, 491–511.

Gosman, A.D., Watkins, A.P., 1977. A computer prediction method for turbulent flow and heat transfer in piston/cylinder assemblies. In: First Symposium on Turbulent Shear Flows, Pennsylvania State University, USA.

Güntsch, E., 1996. Kompression Isotroper Turbulenz im Zylinder – eine Numerische Studie. Dissertation, Lehrstuhl für Fluidmechanik, TU München.

Güntsch, E., Friedrich, R., 1995. Compression of initially isotropic turbulence in a cylinder at low Reynolds number. In: 10th Symposium on Turbulent Shear Flows, Pennsylvania State University, USA.

Hanjalić, K., Hadžić, I., Jakirlić, S., 1999. Modelling the turbulent wall flows subjected to strong pressure variations. ASME J. Fluids Eng. 121 (1), 57–64.

Hanjalić, K., Jakirlić, S., 1998. Contribution towards the second-moment closure modelling of separating turbulent flows. Comput. Fluids 22 (2), 137–156.

Hanjalić, K., Jakirlić, S., Hadžić, I., 1997a. Expanding the limits of equilibrium second-moment turbulence closures. Fluid Dyn. Res. 20, 25–41.

Hanjalić, K., Hadžić, Pascal, H., Jakirlić, S., Tropea, C. 1999a. Study and Modelling of Near-Wall Turbulence in IC Engines. Joulle III Final Report, Contract JOF3CT95-0017.

Hirai, S., Takagi, T., Matsumoto, M., 1988. Predictions of the laminarisation phenomena in an axially rotating pipe flow. ASME J. Fluids Eng. 110, 424–430.

Hunt, J.C.R., 1978. A review of the theory of rapidly distorted turbulent flows and its applications. Fluid Dyn. Trans. 9, 121–152.

Jakirlić, S., Hanjalić, K., Tropea, C., Volkert, J. 1998. On the computation of rotating and swirling confined flows with second-moment closure models. In: Seventh Symposium on Flow Modelling and Turbulence Measurements, Tainan, Taiwan.

Keller, J., Volkert, J., Tropea, C. 1998. Influence of axial compression on a strongly swirling cylinder flow. In: Ninth International Symposium on Applications of Laser Techniques to Fluid Mechanics, Lisbon, Portugal.

Khosla, P.K., Rubin, S.G., 1974. A diagonally dominant second-order accurate implicit scheme. Comput. Fluids 2, 207.

Launder, B.E., Reece, G.J., Rodi, W., 1975. Progress in the development of Reynolds-stress turbulence closure. J. Fluid Mech. 68, 537–566.

Launder, B.E., Sharma, B.I., 1974. Application of the energy-dissipation model of turbulence to the calculation of flow near a spinning disc. Heat Mass Transfer 1, 131–138.

Launder, B.E., Spalding, D.B., 1974. The numerical computation of turbulent flows. Comput. Meth. Appl. Mech. Eng. 3, 269–289.

Le Penven, L., Serre, G. 1993. Homogeneous turbulence submitted to compression: experimental study and modelling. In: Ninth Symposium on Turbulent Shear Flows, Kyoto, Japan.

Lumley's, J.L., 1978. Computational modeling of turbulent flows. Adv. Appl. Mech. 18, 123–176.

Morel, T., Mansour, N.N., 1982. Modelling of turbulence in internal combustion engines. SAE International Congress, Detroit, Michigan, Paper No. 820040.

Murakami, M., Kikuyama, K., 1980. Turbulent flow in axially rotating pipes. ASME J. Fluids Eng. 102, 97–103.

Nishibori, K., Kikuyama, K., Murakami, M., 1987. Laminarization of turbulent flow in the inlet region of an axially rotating pipe. JSME Int. J. 30 (260), 255–262.

Obi, S., Perić, M., Scheuerer, G., 1991. Second-moment calculation procedure for turbulent flows with collocated variable arrangement. AIAA J. 29 (4), 585–590.

Orlandi, P., Fatica, M., 1997. Direct simulations of a turbulent pipe rotating along the axis. J. Fluid Mech. 343, 43–72.

Pascal, H., 1998. Numerical simulation for the study of internal combustion engines flows. LSTM Report, University Erlangen-Nuremberg, Germany.

Patankar, S.V., Spalding, D.B., 1972. A calculation procedure for heat, mass and momentum transfer in three-dimensional parabolic flows. Int. J. Heat Mass Transfer 15, 1787–1806.

Reich, G., Beer, H., 1989. Fluid flow and heat transfer in an axially rotating pipe – I. Effect of rotation on turbulent pipe flow. Int. J. Heat Mass Transfer 32 (3), 551–562.

Reynolds, W.C. 1980. Modelling of fluid motion in engines – an introductory overview. In: Mattavi, Amman, (Eds.), Combustion Modelling in Reciprocating Engines. Plenum Press, New York, pp. 41–68.

Rhie, C.M., Chow, W.L., 1983. Numerical study of the turbulent flow past an airfoil with trailing edge separation. AIAA J. 21 (11), 1525–1532.

Schmid, M. 1996. Systematische Untersuchung von Turbulenzmodellen zweiter Ordnung zur Vorhersage homogener turbulenz, Diplomarbeit, Friedrich-Alexander Universität Erlangen-Nürnberg.

Schmitt, L., 1982. Numerische Simulation Turbulenter Grenzschichten (LES). Teil 1: Grundlagen. Lehrstuhl für Fluidmechanik, TU München, Bericht Nr 82/2.

Schumann, U., Sweet, R.A., 1976. A direct method for the solution of Poisson's equation with Neumann's boundary conditions on a staggered grid of arbitrary size. J. Comp. Phys. 20, 171–182.

Speziale, C.G., Sarkar, S., Gatski, T.B., 1991. Modelling the pressure–strain correlation of turbulence: an invariant dynamical systems approach. J. Fluid Mech. 227, 245–272.

Stone, H.L., 1968. Iterative solution of implicit approximations of multi-dimensional partial differential equations. SIAM J. Numer. Analysis 5 (3), 530–558.

Volkert, J., 1999. Experimentelle und numerische Studie komprimierter Drallströmungen. Ph.D. Thesis, University Erlangen-Nuremberg.

Volkert, J., Tropea, C., Domann, R., Hübner, W. 1996. Combined application of PIV and LDA to swirling flows under compression. In: Eighth International Symposium on Applications of Laser Techniques to Fluid Mechanics, Lisbon, Portugal.

White, F.M., 1974. Viscous fluid flow. McGraw-Hill, NewYork.

Wu, C.T., Ferziger, J.H., Chapman, D.R., 1985. Simulation and modelling of homogeneous, compressed turbulence. In: Fifth Symposium on Turbulent Shear Flows, Ithaca, NY, USA.